J. Fluid Mech. (2007), *vol.* 592, *pp.* 1–21.
doi:10.1017/S0022112007007707 Printed in the United Kingdom

Wake states of a tethered cylinder

J. CARBERRY AND J. SHERIDAN

Department Mechanical Engineering, Monash University 3800, Australia
josie.carberry@eng.monash.edu.au

(Received 9 January 2006 and in revised form 29 May 2007)

This paper describes an experimental investigation of a buoyant, $m^* < 1$, tethered cylinder which is free to move in an arc about its pivot points. The response of the cylinder, in particular its layover angle and flow-induced motion, is considered for a range of flow velocities and mass ratios. At pertinent parameters, the flow fields were also measured using particle image velocimetry (PIV). At lower mass ratios, $0.54 \leqslant m^* \leqslant 0.72$, two distinct states are observed, the low-amplitude and upper states. The transition from the low-amplitude state to the upper state is characterized by abrupt jumps in the amplitude of oscillation, the mean tether angle and the drag coefficient as well as distinct changes in the cylinder's wake. At higher mass ratios, the jump does not occur; however, as m^* approaches unity at low flow velocities the cylinder's motion is more periodic than that observed at lower m^*. The flow fields indicate that the low-amplitude state exhibits a 2S Kármán wake. The wake of the upper state has long shear layers extending well across the wake centreline, is not fully symmetric and is often consistent with either the 2P or P + S shedding modes. There is a collapse of the response data, in particular an excellent collapse of the mean layover angle, when the response parameters are plotted against the buoyancy Froude number, $Fr_{buoyancy} = U/((1 - m^*)gD)^{0.5}$. When the data collapses, the two states described above are clearly delineated.

1. Introduction

Instabilities generated by fluid flow over a body can result in large-scale motion of the body. A number of previous investigations have considered the case of a cylinder constrained to move transverse to the flow (e.g. Govardhan & Williamson 2000), or a cylinder with two-dimensional motion in the transverse and in-line directions (e.g. Jauvtis & Williamson 2004). A closely related problem is that of a rigid tethered cylinder (figure 1), where the cylinder is free to move in an arc about its pivot points. Despite the relevance of this case to the response of tethered bodies submerged in a steady current, this problem received almost no attention until the numerical investigations of Ryan, Thompson & Hourigan (2002, 2003). In this experimental investigation, the response of a tethered buoyant cylinder to a range of flow velocities is analysed. The effect of varying the mass ratio m^*, where m^* is the mass of the body normalized by the mass of fluid it displaces, was also investigated.

The fluid–structure interaction of a cylinder moving relative to a free stream results in significant modification of both the forces on the cylinder and the structure of the near wake. Typically, either the cylinder motion is 'free', and occurs in response to flow-induced forces, or the motion of the cylinder is externally driven. Until recently, the majority of investigations have focused on cylinder motions that are either transverse or in-line with the free stream.

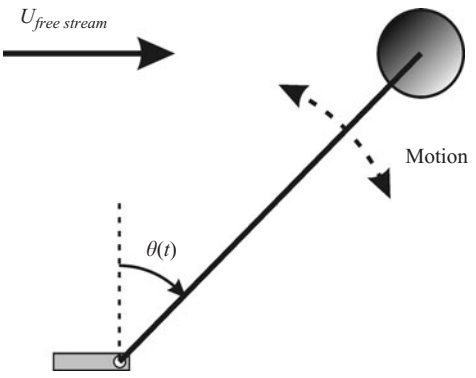

FIGURE 1. Schematic of the tethered cylinder in the free stream.

An elastically mounted cylinder constrained to move transverse to the flow has been found to exhibit two or three different response branches (Govardhan & Williamson 2000), where the number of branches depends on the mass-damping of the system. Govardhan & Williamson (2002) also investigated a lightly damped non-elastically mounted system by removing the springs that had previously provided the mechanical restoring force (i.e. the case where $k=0$). Without a mechanical restoring force, the response of the system was found to depend primarily on the mass ratio m^*, and large oscillations were observed only for m^* less than a critical value, $m^*_{CRIT}=0.54$. The cylinder displayed two states: for $m^* > m^*_{CRIT}$ the cylinder oscillations were very small or the cylinder was essentially stationary, whereas for $m^* < m^*_{CRIT}$ large-amplitude oscillations occurred. The change in oscillation amplitude corresponded to a change in vortex-shedding mode from 2S for the small oscillations, to 2P with long extended shear layers for the large-amplitude oscillations. Similar changes in the mode of vortex shedding were observed for the response branches of the elastically mounted cylinder, with m^*_{CRIT}, also equal to 0.54, corresponding to an apparently infinite extension of the upper response branch. Jauvtis & Williamson (2004) found similar response branches for their two-dimensional cylinder motion with a corresponding m^*_{CRIT} value of 0.52. The precise value of m^*_{CRIT} appears to be a function of the geometry of the particular system and the Reynolds-number regime; for example Govardhan & Williamson (2005) predict a critical mass ratio of 0.6 for a tethered sphere, compared to $m^*_{CRIT}=0.54$ for the transverse cylinder motion at similar values of *Re*. Results of numerical modelling at Reynolds numbers between 100 and 200 by Shiels, Leonard & Roshko (2001) and Ryan (2004) indicate that m^*_{CRIT} may be significantly smaller at lower *Re*.

Ongoren & Rockwell (1988) found that a cylinder undergoing forced sinusoidal oscillations at a range of inclination angles, and over a range of oscillation frequencies, exhibits a number of different shedding modes. Transverse oscillations (90° inclination) resulted in stable antisymmetric wakes; however, as the inclination angle decreased towards 0°, i.e. in-line oscillations, symmetric wake modes also occurred. The wakes exhibited continual switching between symmetric and antisymmetric modes of vortex shedding, with the antisymmetric modes becoming less dominant as the inclination angle decreased. This high level of mode competition indicates that the forced inclined oscillations did not produce a single stable wake state.

For very long or infinite tether lengths, the motion of a tethered cylinder can approach that of the in-line or transverse cases; however, typically the direction of

the cylinder's motion is at an angle to the free stream. One of the interesting features of a tethered body is that the geometry of the cylinder's motion relative to the free stream changes with the mean tether angle.

The majority of the previous work on tethered bodies has focused on spheres or buoys, typically involving interaction with a free surface and surface waves. In the absence of these additional factors, Govardhan & Williamson (2005) found that a fully submerged sphere exhibits large-scale oscillations over a wide range of reduced velocities. At higher reduced velocities, the response of the sphere is not locked-on to the natural structural frequency and the oscillation frequency is significantly less then the corresponding Strouhal frequency of a stationary sphere.

To date, the case of a tethered cylinder has received relatively little attention, with the exception of the two-dimensional numerical investigations of Ryan *et al.* (2002, 2004*a*, *b*) and Ryan 2004. At a mass ratio of $m^* = 0.833$ and a constant Reynolds number of 200, Ryan *et al.* (2002, 2004*a*) observed that the mean tether angle increased smoothly with increasing reduced free-stream velocity. As the mean tether angle increased, the drag coefficient remained essentially constant and was similar to that of a stationary cylinder, the exception being at high reduced velocities where there was a slight decrease in the drag coefficient. At low reduced velocities, corresponding to an essentially vertical tether, extremely small cylinder oscillations were observed. As the reduced velocity increased, the oscillations grew in amplitude, but remained less than 0.2 cylinder diameters in amplitude. Numerical experiments looking at the effect of mass ratio (Ryan 2004) showed the existence of a critical mass ratio below which the cylinder 'jumps' to large-amplitude oscillations at higher Froude numbers. As described previously for other systems, this large-amplitude response appears to extend to infinite flow velocities. Ryan (2004) showed that the value of m^*_{CRIT} is a function of tether length, decreasing exponentially with increasing L^*. At $L^* = 4.6$ and $Re = 200$, m^*_{CRIT} was predicted to be 0.41, which is much lower than the value found in the current work.

Previous numerical investigations of the response of a tethered cylinder were conducted at relatively low Reynolds numbers where it is reasonable to assume a two-dimensional flow. The experimental investigation reported in this paper seeks to address the following questions at higher Reynolds numbers, where the flow is inherently three-dimensional:

How does the response of the tethered cylinder vary with free-stream velocity?
What is the effect of varying the mass ratio (or buoyancy force) of the cylinder?
Does the tethered cylinder system exhibit distinct wake states that are comparable to the wake states (or response branches) observed in similar oscillatory systems?

The variation of the response with free-stream velocity is presented for a range of mass ratios and then the effect of mass ratio is considered in more detail.

2. Experimental method

A cylinder, 16.2 mm in diameter and 594 mm long, was tethered at each end with carbon fibre rods. The rods were 75.0 mm long and 3 mm in diameter, giving a normalized tether length to cylinder diameter ratio, $L^* = L/D$, of 4.6. Both the cylinder and the tethers are rigid and there is no relative motion between them. The tether is located at the pivot point with precision bearings and the cylinder is free to rotate about the pivot point (figure 1). The pivot point is located approximately halfway between the free surface and the bottom of the channel, thus neither the bottom

of the channel nor the free surface is expected to affect the motion of the cylinder. Experiments were performed for a range of different mass ratios, $0.54 \leqslant m^* \leqslant 0.97$, where by definition in all cases the cylinder experiences a positive upwards buoyancy force. During each set of experiments the flow velocity, U, increased from zero to $0.46\,\mathrm{m\,s^{-1}}$, corresponding to a maximum Reynolds number of 7390. The experiments were conducted in the FLAIR free-surface water channel at Monash University, which has a working section of $4000\,\mathrm{mm} \times 600\,\mathrm{mm} \times 535\,\mathrm{mm}$ (length $\times$ width $\times$ height) and turbulence levels of less than 1 %.

The motion of the cylinder is one-dimensional and is described by the angle of the tether from the vertical axis, $\theta(t)$. A 25 Hz PAL video camera was used to track the position of the cylinder, and the system was calibrated to correct for optical distortion. For all experiments, the frequencies of interest were less than 5 Hz and were thus well resolved by the 25 Hz sampling frequency. At each free-stream velocity, the sampling period was at least 328 s, resulting in a minimum of 8196 data points. The mean tether angle θ_{mean}, the standard deviation of the cylinder position θ_{std} and the maximum variation in the cylinder cyclic motion θ_{max} (half the peak to peak value) were calculated from $\theta(t)$. The parameters describing the motion of the cylinder, θ_{std} and θ_{max} are normalized using the angle subtended by the cylinder diameter, θ_D. Spectral analysis of the data was performed using spectral averaging with a bin size of 1024 data points.

Flow fields were measured using digital particle image velocimetry (PIV). The flow field was illuminated using a pair of pulsed mini YAG New Wave® lasers, and image pairs, corresponding to consecutive laser pulses, were recorded on a 4 megapixel, RedLake® ES4.0 double exposure camera using an EPIX® image acquisition card and software. The timing of the laser and camera triggering was controlled by an in-house timing unit, with an estimated accuracy of 1 μs. The flow was seeded with silver-coated glass spheres, nominal diameter 12 μm from Potters Industries, and all PIV images were taken in a plane corresponding to the centre of the cylinder. The PIV images were processed using in-house software which incorporated adaptive grid algorithms. The data were processed using and initial window size of 64 pixels and a final window size of 16 pixels with 50 % overlap. The flow fields are presented using both instantaneous and mean vorticity fields, where the mean vorticity fields are calculated from the average of 230 instantaneous flow fields.

The framing rate of the PIV camera (5 Hz) was not adequate to resolve the motion of the cylinder, therefore both the PIV camera and the video camera measuring the displacement were used in the experiments to determine the flow fields corresponding to different cylinder responses. Careful calibration of these two cameras and subsequent post-processing allowed the time at which each flow field was measured to be identified within the displacement time trace.

2.1. *Force balance*

Consideration of the force components acting on the cylinder allows the magnitude of the fluid forces to be inferred directly from the position of the cylinder. Typically, the wake behind a circular cylinder has symmetry about its centreline, for example a Kármán wake, and there is an equal distribution of positive and negative vorticity downstream of the cylinder, with a zero net lift force. By assuming a net zero lift force, $C_L \approx 0$, for the tethered cylinder, both the mean tension in the tether, T, and the mean drag force coefficient, C_D, can be calculated from θ_{mean} and the buoyancy

force, $B = (1 - m^*)\, m_d g$, where m_d is the mass of fluid displaced by the cylinder:

$$T = \frac{(1 - m^*)\, m_d\, g}{\cos(\theta_{mean})}, \tag{1}$$

$$C_D = \frac{(1 - m^*)\, \pi D g \tan(\theta_{mean})}{2U^2}. \tag{2}$$

The natural structural frequency of the system, f_N, is analogous to that of a pendulum and depends on the tension in the tether. Thus, f_N varies with the mean tether angle:

$$f_N = f_{N\,water} = \frac{1}{2\pi}\sqrt{\frac{(1 - m^*)g}{(m^* + C_A)L^* D \cos(\theta_{mean})}}. \tag{3}$$

In (3), C_A is the idealized added mass coefficient, where for a circular cylinder $C_A = 1$.

The findings of a parallel numerical study on the tethered cylinder (Ryan *et al.* 2004*b*) indicate that the mean lift force is essentially zero except for cases where the cylinder oscillation amplitude is large. For large cylinder oscillations, $\theta^*_{std} > 0.3$, it is anticipated that there is a mean negative lift force on the cylinder. In these cases, our calculations that incorporate the assumption of $C_L \approx 0$ will overestimate both the tension in the tether and the natural structural frequency of the system.

The reduced velocity is given by $U^* = U/f_N D$, where D is the diameter of the cylinder, U is the free-stream velocity and f_N is the natural structural frequency of the tethered body in water. Previous investigations of flow-induced vibrations have commonly used the reduced velocity as the non-dimensional variable against which the response variables are plotted. However, in this investigation the natural structural frequency varies with θ_{mean} and therefore U^* is not an independent variable. Moreover, the calculation of f_N incorporates the assumption that the mean lift force is zero. Thus the initial plots are presented in figure 2 in terms of U^* so that the current results can be related to the existing literature. We present and discuss our results in figure 2 in terms of the dimensionless Froude number, $Fr_{gravity} = U/(gD)^{0.5}$ rather than U^*. The subscript 'gravity' has been added to this Froude number to differentiate it from the buoyancy Froude number which will be discussed later in the paper. In these experiments, both gravity and the cylinder diameter are constant so $Fr_{gravity}$ varies directly with the free-stream velocity. The tethered cylinder has no mechanical restoring force, but it does have a 'fluid/buoyancy' restoring force owing to the force balance between the mean fluid forces (drag and lift) and the buoyancy force.

3. Results and discussion

These experiments consider the effect of varying two different experimental parameters: the $Fr_{gravity}$ (i.e. the free-stream velocity of the channel, U) and the mass ratio m^*. Varying $Fr_{gravity}$ alters the ratio of the inertial force to the gravitational or buoyancy forces whereas varying m^* directly alters the buoyancy force of the cylinder.

In figure 2, the response parameters, θ_{mean}, θ_{std}/θ_D, θ_{max}/θ_D and C_D, are presented as functions of $Fr_{gravity}$ for ten different mass ratios, $m^* = 0.54 \rightarrow 0.97$. As expected, these figures show that the response is a function of mass ratio; at lower m^* values, $m^* \leqslant 0.72$, there is an abrupt increase in these response parameters as the free-stream velocity increases. Hereinafter, this increase will be described as a 'jump' and will be discussed in detail later in this section. The jump in these parameters is consistent

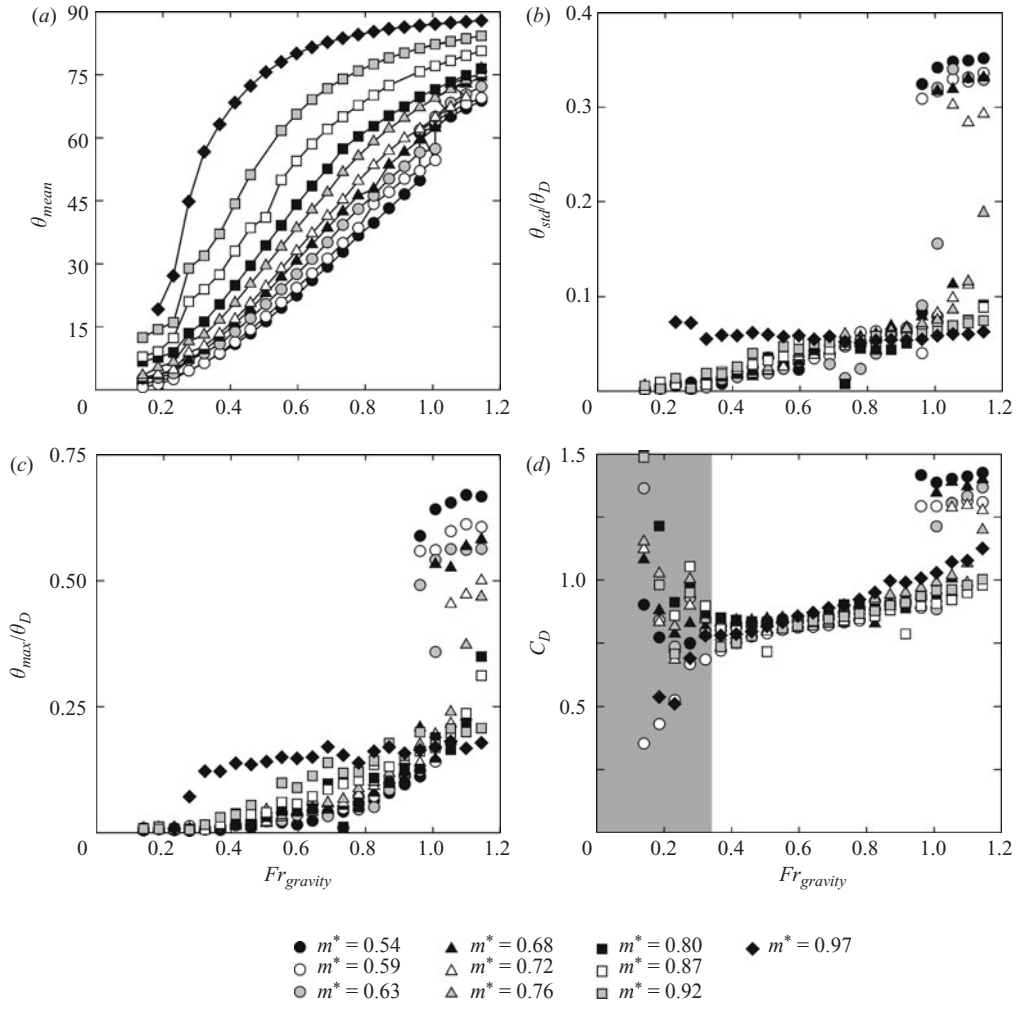

FIGURE 2. Parameters describing the response of the cylinder as a function of $Fr_{gravity}$ for $m^* = 0.54$ to 0.97. (*a*) θ_{mean}, (*b*) θ_{std}/θ_D, (*c*) θ_{max}/θ_D and (*d*) C_D.

with that observed in the two-dimensional numerical experiments of Ryan (2004) within a lower-Reynolds-number regime.

3.1. *Mean layover angle, oscillation amplitude and drag*

The variation of the mean layover angle of the tether, θ_{mean}, as $Fr_{gravity}$ increases is shown in figure 2(*a*) for all values of m^* considered in this study. These results clearly show that θ_{mean} increases with both $Fr_{gravity}$ and m^*. At lower values of m^* (0.54–0.72) there is an upward jump in θ_{mean} between $Fr_{gravity} = 0.96$ and 1.14. With the exception of this jump, the mean layover angle increases smoothly with increasing $Fr_{gravity}$, or in other words the cylinder is gradually 'pushed over' as the inertia of the fluid increases. The smooth variation of θ_{mean} with $Fr_{gravity}$ is consistent with the idealized variation for a constant drag coefficient and is also consistent with the numerical results of Ryan *et al.* (2002, 2004*a*, *b*) and Ryan (2004) at a lower Reynolds number, $Re = 200$.

At the highest values of m^*, as the cylinder approaches the neutrally buoyant condition ($m^* = 1$), θ_{mean} increases rapidly as $Fr_{gravity}$ is increased from rest, and thus

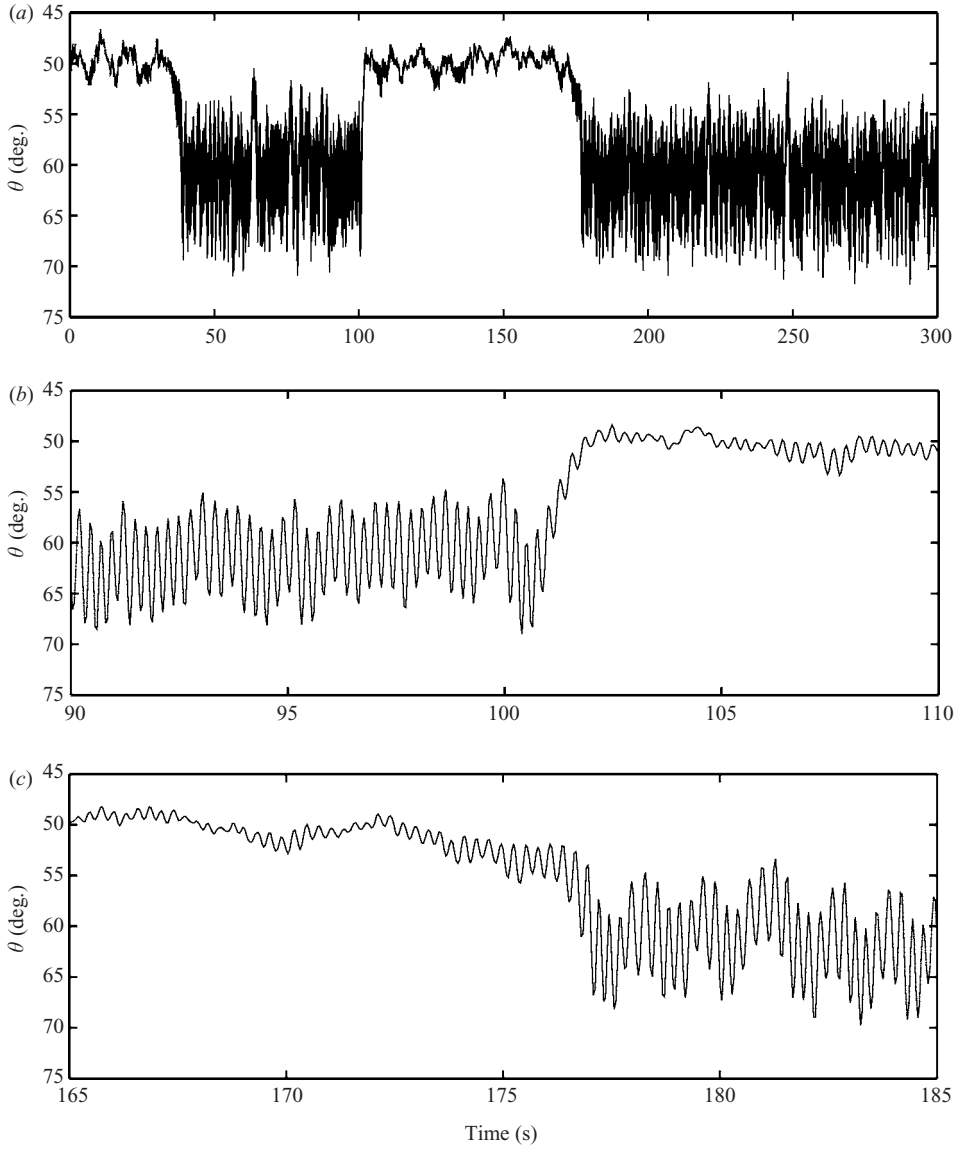

FIGURE 3. Cylinder position as a function of time at $m^* = 0.54$ and $U = 0.38\,\mathrm{m\,s^{-1}}$. $Fr_{gravity} = 0.96$. (*a*) A number of self-excited transitions corresponding to changes in both θ_{mean} and oscillation amplitude are evident. (*b*) The transitions from large to small oscillations and (*b*) small to large oscillations shown in more detail.

even at moderate $Fr_{gravity}$ values the majority of the cylinder motion is transverse to the free stream. Conversely, at lower m^* values when the relative mass of the cylinder is lighter, θ_{mean} is smaller. The jump in θ_{mean} at lower m^* values occurs after θ_{mean} has increased through 45°, which is after the point at which the dominant component of the cylinder's motion switches from in-line to transverse.

The amplitude of the cylinder's flow-induced motion is presented using two different parameters: the statistical standard deviation of the cylinder about its mean position, θ_{std}, and the amplitude of the largest oscillation, θ_{max}. Both θ_{std} and θ_{max} are normalized by the angle subtended by the cylinder's diameter, θ_D, and the variation of these two

parameters with $Fr_{gravity}$ and m^* is shown in figures 2(*b*) and 2(*c*), respectively. θ_{std}/θ_D for the tethered system is directly equivalent to an oscillation amplitude A/D, where A is the amplitude of the standard deviation tangent to the cylinder's motion and D is the diameter of the cylinder. At the lowest flow velocities, very small-amplitude (<0.01 % of the cylinder's diameter) low-frequency (<0.1 Hz) motion was detected, an example of this motion is shown in figure 2(*a*); however, for practical purposes the cylinder is essentially stationary. As $Fr_{gravity}$ increases, the cylinder exhibits small-scale motion and the amplitude of these oscillations grows with increasing $Fr_{gravity}$. As m^* increases, the onset of small-scale motion occurs at lower values of $Fr_{gravity}$, but this onset does not appear to be linked to a particular mean layover angle.

For $m^* \leqslant 0.72$, an abrupt jump in the oscillation amplitude is observed, where the jumps in θ_{std}/θ_D and θ_{max}/θ_D (figure 2*b*, *c*), correspond to the jump in θ_{mean}. The abrupt changes in both the mean layover angle and the oscillation amplitude indicate that the jump is a transition between two different wake states; the corresponding vorticity fields will be discussed in § 3.3. Examination of the $\theta(t)$ traces, described in detail later in this paper, shows that the transition between these two states can occur as $Fr_{gravity}$ varies during an experiment or the cylinder may also undergo self-excited transitions at a constant value of $Fr_{gravity}$. When the self-excited transitions occur at a constant $Fr_{gravity}$, the data presented in figure 2 are split into segments that are representative of the states either side of the jump. The link between the abrupt changes in the oscillation amplitude and the mean layover angle is also clearly evident in the $\theta(t)$ traces and is characteristic of the jump.

For the majority of the data presented in figure 2(*b*, *c*), the magnitude of θ_{max}/θ_D is almost twice (i.e. significantly more than $\sqrt{2}$ times) that of θ_{std}/θ_D, indicating that there is significant temporal variation in the oscillation amplitude. The standard deviation of the large oscillations after the jump ($m^* \leqslant 0.72$) in figure 2(*b*) shows that on average the amplitudes are only slightly larger for the lighter cylinders. However in figure 2(*c*), the variation of θ_{max}/θ_D after the jump shows a much stronger dependence on m^*.

In figure 2(*d*), the drag coefficient, calculated from (2), is plotted as a function of $Fr_{gravity}$ for a range of m^* values. When C_D is calculated from small values of θ_{mean}, the error is magnified because the error in the measurement of θ_{mean} is a significant percentage of the actual value causing wide scatter in the values of C_D for $Fr_{gravity}$ <0.37. This region of significant measurement error is shaded in figure 2(*d*). The data in figure 2(*d*) show that the jump in θ_{mean} and θ_{std}/θ_D also corresponds to a jump in C_D. For values of $Fr_{gravity}$ below the jump, or for m^* where the jump does not occur, the drag coefficient is almost constant, increasing gradually with increasing Re. The value of C_D before the jump is approximately 0.9, which is actually lower than the corresponding value for a stationary cylinder at these Reynolds numbers (C_D(stationary) = 0.95 – 1.2, Zdravkovich 1997). After the jump, the drag coefficient is in the range $C_D = 1.3$ – 1.4, and appears to be relatively independent of $Fr_{gravity}$. The values of C_D before the jump increase slightly with increasing $Fr_{gravity}$. In this region, the Reynolds number increases from ≈1000 to 7000 and the increase in C_D is consistent with the variation with Re for a stationary cylinder. However, at all Re, the values of C_D before the jump remain lower than the corresponding values for the stationary cylinder. The cylinder cannot be fitted with end plates because of the relatively massive moments of inertia generated by such plates. Thus, it is possible that end effects may contribute to the relatively low values of C_D. The fact that C_D remains essentially constant either side of the jump (taking into account Re effects) is an interesting feature of this system.

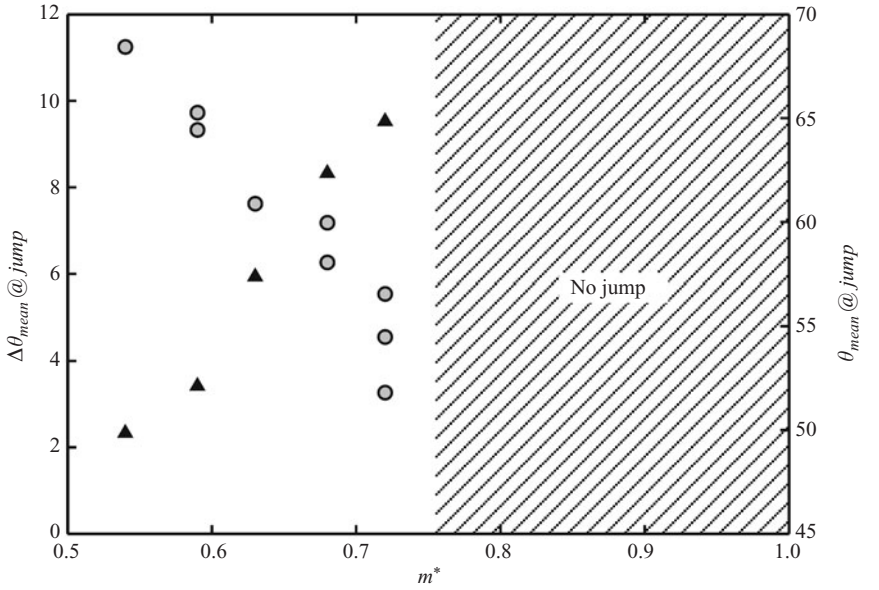

FIGURE 4. Variation of the changes in the mean layover angle at the jump with m^*. ○, magnitude of the jump in θ_{mean} at transition, $\Delta\theta_{mean}$@*jump*; ▲, value of θ_{mean} at which the jump occurs, θ_{mean}@ *jump*.

3.2. *Variation with m^*: three different regimes*

The results shown in figure 2, and examination of the associated time traces shown in figures 3, 5 and 6, indicate that as the mass of the cylinder varies there are three identifiable m^* regimes:

1. At lower $m^*(0.54 \leqslant m^* \leqslant 0.72)$ there is a jump in the response parameters: both θ_{mean} and the amplitude of the cylinder's motion increase gradually as $Fr_{gravity}$ increases until there is an abrupt jump in θ_{mean}, θ_{std}/θ_D and C_D.
2. At intermediate values of $m^*(0.76 \leqslant m^* \leqslant 0.87)$ the jump does not occur: θ_{mean} and θ_{std}/θ_D increase smoothly with $Fr_{gravity}$ and the drag coefficient remains close to $C_D \approx 0.9$. The cylinder's motion is periodic, but there is some variation in the amplitude of oscillation (e.g. figure 5*b*, *c*).
3. As m^* approaches unity ($m^* \geqslant 0.92$) the motion of the cylinder is very periodic (e.g. figure 6*a*) at lower $Fr_{gravity}$, but as $Fr_{gravity}$ increases, the motion becomes more disorganized. As for intermediate values of m^*, a jump is not observed.

The m^* regimes are now discussed in more detail.

3.2.1. *The jump: lower m^** $(0.54 \leqslant m^* \leqslant 0.72)$

The characteristic displacement trace shown in figure 3, at $m^* = 0.54$ and $Fr_{gravity} = 0.96$, illustrates the variation of the layover angle θ and the oscillation amplitude either side of the transition. The vertical axis is inverted to represent the physical orientation of the cylinder in the experiments, i.e. the lower θ values, where the cylinder is more upright, are plotted above the higher θ values where the cylinder is more sloping. The displacement trace in figure 3(*a*) shows three self-excited transitions occurring within a 300 s time period. The transition from large oscillations to small oscillations at $t \approx 101$ s and the transition back to large oscillations at $t \approx 177$ s are

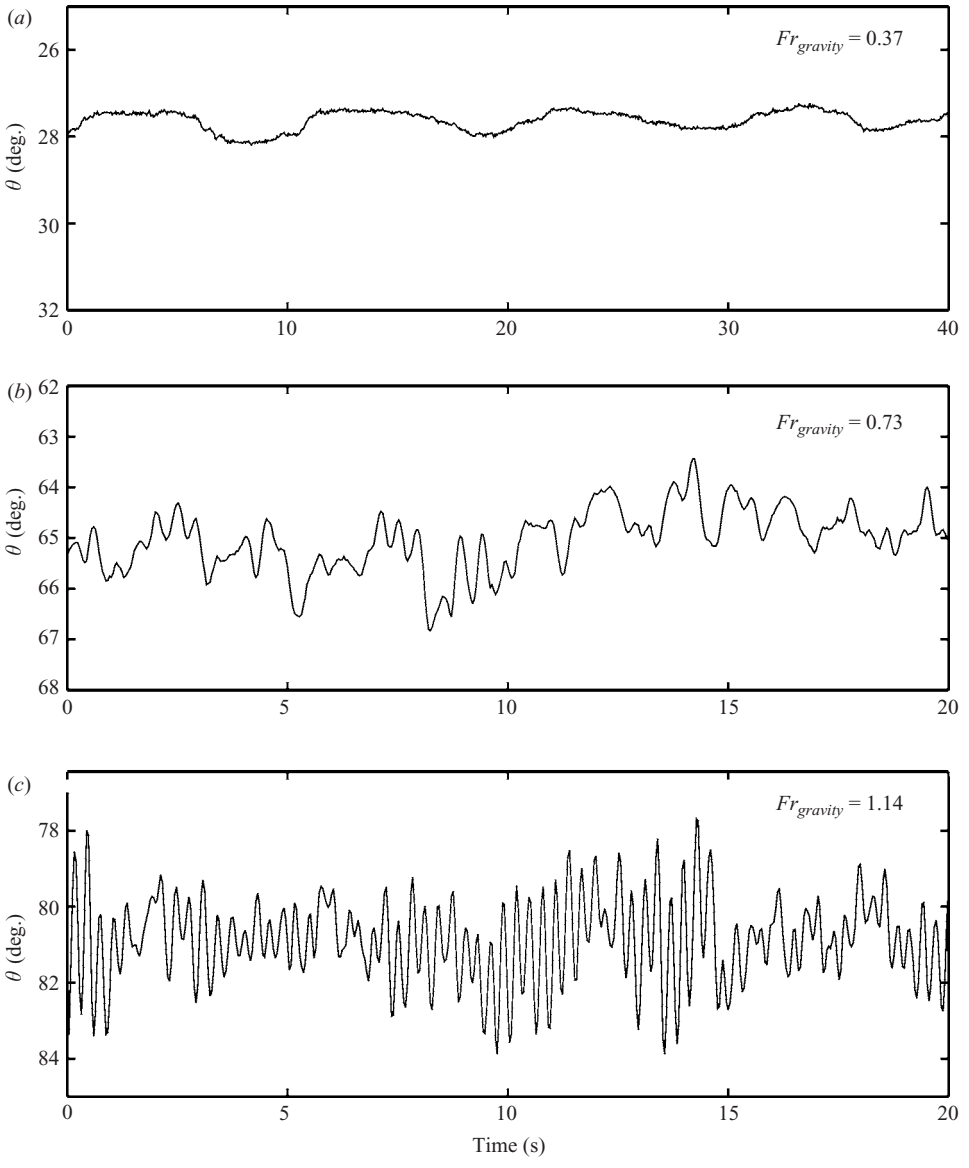

FIGURE 5. Cylinder position as a function of time at $m^* = 0.87$ and for three different flow velocities/Froude numbers: (*a*) at very low flow velocities, $U = 0.15\,\mathrm{m\,s^{-1}}$, (*b*) $U = 0.29\,\mathrm{m\,s^{-1}}$ and (*c*) at higher flow velocities, $U = 0.46\,\mathrm{m\,s^{-1}}$. Note the difference in the time scale between the very small low-frequency motion at $U = 0.15\,\mathrm{m\,s^{-1}}$ and the other time traces.

magnified in figures 3(*a*) and 3(*b*), respectively. These figures clearly demonstrate that the abrupt increase in θ_{mean} corresponds to an increase in the oscillation amplitude and vice versa.

The jump described above occurred at all mass ratios between $m^* = 0.54$ and 0.72, where $m^* = 0.54$ was the lightest mass ratio investigated. As m^* increases, both the point at which the jump occurs ($\theta_{mean}@jump$) and the magnitude of the change in the mean layover angle during the jump ($\Delta\theta_{mean}@jump$) changed. Figure 4 shows the variation with m^* of '$\theta_{mean}@jump$', taken as the lowest θ value from which the

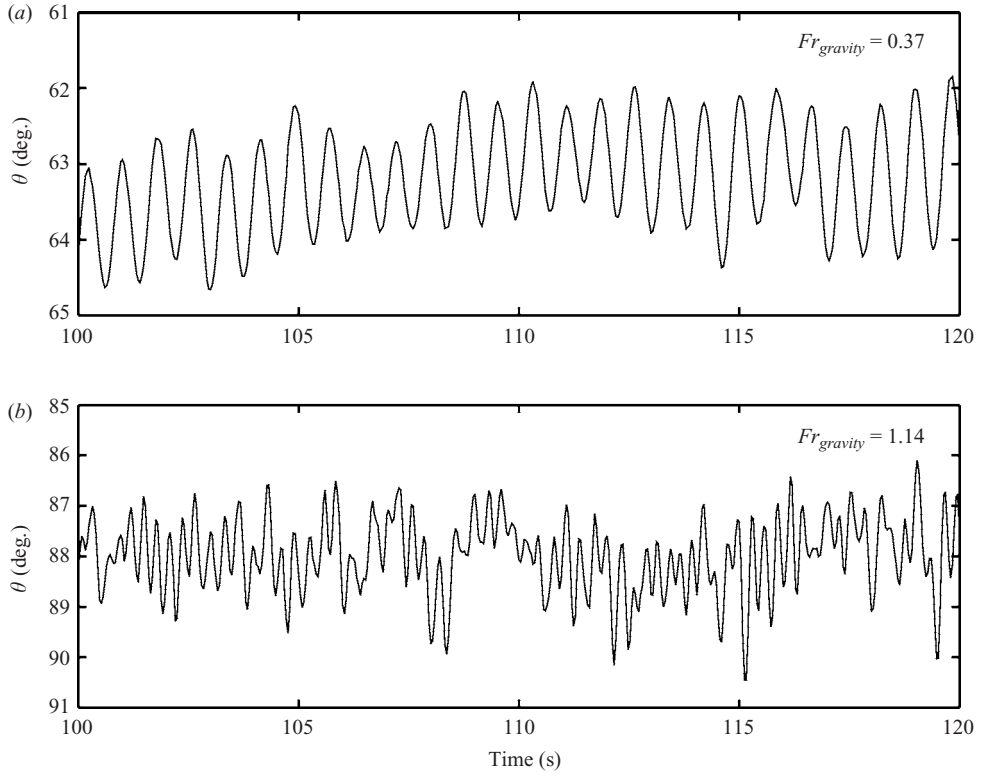

FIGURE 6. Cylinder position as a function of time at $m^* = 0.97$. (*a*) At lower flow velocities $U = 0.15\,\mathrm{m\,s^{-1}}$, the motion is very periodic while at higher velocities, $U = 0.46\,\mathrm{m\,s^{-1}}$, (*b*) the motion becomes significantly less organized.

upward jump occurred, and '$\Delta\theta_{mean}@jump$'. In some cases there are a number of '$\Delta\theta_{mean}@jump$' points for a single m^* value as a self-excited transition occurred at more than one free-stream velocity. As m^* increases from 0.54 to 0.72, the mean layover angle at which the jump occurs increases from 49.9° to 64.8° and, as shown in figure 2(*a*), there is also a corresponding increase in the value of $Fr_{gravity}$ at which the jump occurs. In contrast, the magnitude of the change in the mean layover angle at transition decreases as m^* increases towards 0.72. The essentially linear decrease in $\Delta\theta_{mean}@jump$ indicates that as m^* increases, the system is tending towards a point at which there is no jump, corresponding to the shaded region in figure 4. At $m^* = 0.76$, there is not a clearly defined jump in θ_{mean}; however, there is significant modulation of the amplitude at high flow velocities.

3.2.2. *No jump: intermediate values of* m^* $(0.76 \leqslant m^* \leqslant 0.87)$

The jump in θ_{mean} and oscillation amplitude does not occur at intermediate mass ratios, $0.76 \leqslant m^* \leqslant 0.87$ and, as shown in figures 2(*a*) and 2(*b*), both the mean layover angle and the oscillation amplitude increase smoothly with increasing free-stream velocity. At higher flow velocities, the motion is oscillatory, but, as shown in figure 5(*c*), is significantly less organized than the highly periodic oscillations after the jump in figure 4. At lower velocities, the motion is essentially consistent with that observed at lower m^* before the jump: at very low velocities there are extremely small slow oscillations (figure 5*a*), as the free-stream velocity is increased beyond

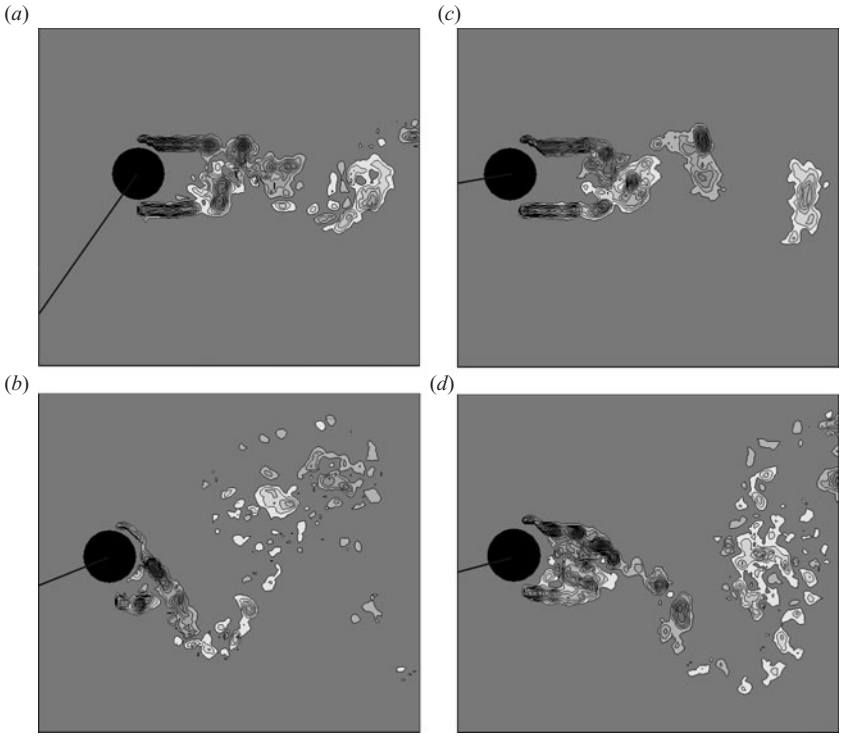

FIGURE 7. Instantaneous vorticity fields at $m^* = 0.54$ (a) at low Froude number, $Fr_{gravity} = 0.78$, before the jump and (b) at higher Froude number $Fr_{gravity} = 1.14$, after the jump. At higher m^* there is no jump, illustrated in (c) $m^* = 0.87$ at $Fr_{gravity} = 1.14$. The highest m^* at which the jump occurred was $m^* = 0.72$, shown in (d) after the jump at $Fr_{gravity} = 1.14$.

the onset of small-scale oscillations the motion is relatively disorganised (figure 6b). The magnitudes of the corresponding spectral peaks confirm these trends and will be discussed in more detail later in the paper.

3.2.3. *As* $m^* \rightarrow$ *unity:* $m^* \geqslant 0.92$

As m^* approaches unity there is a change in the motion of the cylinder at lower values of $Fr_{gravity}$. As $Fr_{gravity}$ is increased from zero the cylinder quickly moves to relatively high values of θ_{mean} and, as shown in figure 6(a), the motion is remarkably periodic. These highly periodic low-frequency oscillations did not occur at mass ratios below $m^* = 0.92$, for example see figure 5 where $m^* = 0.87$. The amplitudes of these very periodic oscillations are higher than for lower mass ratios at these values of $Fr_{gravity}$, but are similar in amplitude to the oscillations at the same θ_{mean} and lower m^* values. Thus, the early onset of highly periodic motion shown in figure 6(a) may be linked to the relatively high layover angles as m^* approaches unity. As $Fr_{gravity}$ increases further, θ_{mean} approaches 90° and, while θ_{std}/θ_D and θ_{max}/θ_D remain relatively constant, the motion of the cylinder, shown in figure 6(b), is much less periodic and is similar to that observed for intermediate mass ratios at high values of $Fr_{gravity}$. Despite the difference in the cylinder's motion at lower $Fr_{gravity}$ as m^* approaches unity, the drag coefficient remains similar to that at much lower m^* where the periodic motion does not occur.

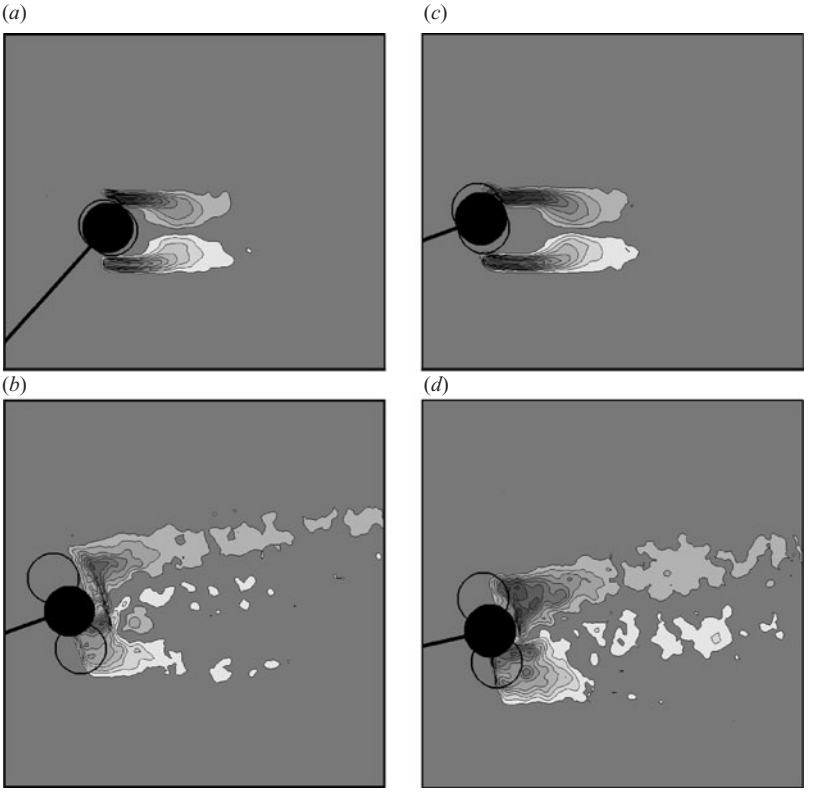

FIGURE 8. Mean vorticity fields at $m^* = 0.54$ (*a*) at low Froude number, $Fr_{gravity} = 0.78$, before the jump and (*b*) at higher Froude number $Fr_{gravity} = 1.14$, after the jump. At higher m^* there is no jump, illustrated in (*c*) $m^* = 0.87$ at $Fr_{gravity} = 1.14$. The highest m^* at which the jump occurred was $m^* = 0.72$, shown in (*d*) after the jump at $Fr_{gravity} = 1.14$.

3.3. *Wake states*

Examination of the flow fields using PIV reveals that the jump in θ_{mean} and θ_{std} corresponds to a change in the mode of vortex shedding. The change in the wakes is clearly evident in both the instantaneous vorticity fields (figure 7) and the mean vorticity fields (figure 8).

At mass ratios where the jump occurs ($m^* \leqslant 0.72$) the wake state at lower $Fr_{gravity}$ values before the jump (figures 7*a* and 8*a*), is the commonly observed Kármán or 2S mode of shedding. Similarly, at higher mass ratios, where the jump is not observed, the Kármán wake persists over the full range of $Fr_{gravity}$ values studied. Thus, despite the large difference in the values of $Fr_{gravity}$, m^* and θ_{mean} for the cases illustrated in figures 7(*a*) and 7(*c*), the modes of vortex shedding are similar both to each other and to that of a stationary cylinder. The similarities are also evident in the corresponding mean fields shown in figures 8(*a*) and 8(*c*).

At mass ratios where the jump is observed, the increase in the cylinder's oscillation amplitude corresponds to a distinctly different mode of vortex shedding. For values of $Fr_{gravity}$ above the jump, the larger oscillation amplitude generates longer shear layers resulting in a wide vertical distribution of vorticity; the wakes after the jump in figures 7(*b*) and 7(*d*) are much wider than the wakes in figures 7(*a*) and 7(*c*) either before the jump or where the jump does not occur. The corresponding mean

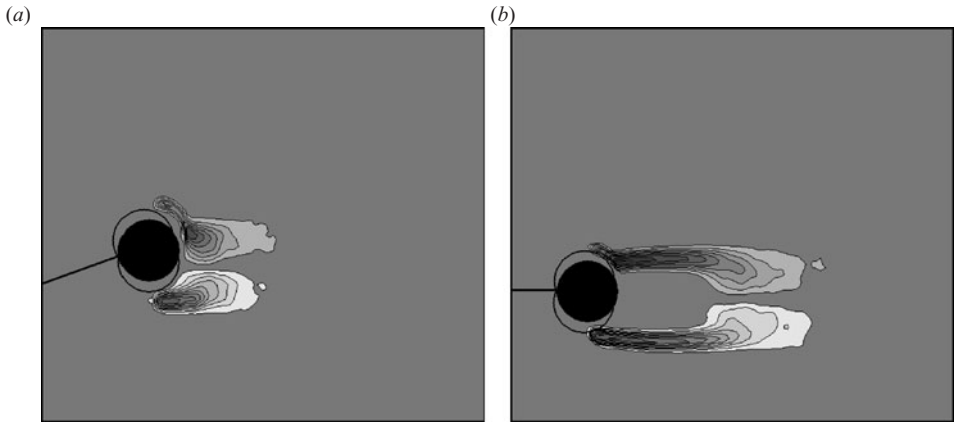

FIGURE 9. Mean vorticity fields at $m^* = 0.97$ (a) at lower Froude number, $Fr_{gravity} = 0.37$, with very periodic cylinder motion and (b) at high Froude number, $Fr_{gravity} = 1.12$, where the cylinder's motion is not very periodic.

vorticity fields in figures 8(b) and 8(d) show that the wake is not fully symmetric and has a distinct upward angle. The angling of the mean wake upwards is consistent with a net negative lift force on the cylinder. The instantaneous wakes show vorticity generated on one side of the shear layer crossing well into the other side of the wake; for example, large quantities of positive vorticity are present in the upper portion of the wake. This type of vorticity distribution promotes the pairing of counter-rotating vortices. In the symmetric wake of a transversely oscillating cylinder, similarly formed wakes result in the 2P shedding mode, with two counter-rotating vortex pairs formed per oscillation cycle. The 2P mode of shedding is observed for both free and forced transverse oscillations at higher values of U^*, lower m^* and higher oscillations amplitudes. The mean vorticity fields of the 2P shedding mode for both the forced and free oscillation (described by Carberry, Sheridan & Rockwell 2005) show characteristic small lobes of oppositely signed vorticity downstream of the main shear layer and close to the wake centreline. These lobes of oppositely signed vorticity are evident in the tethered cylinder wake at $m^* = 0.54$ in figure 8(b); however, the non-symmetry of the wake is more evident in figure 8(d) at $m^* = 0.72$ and the upward angling of the wake appears to have annihilated the lobes. It is not clear whether the wakes after the jump have the 2P mode of shedding; however, these wakes are similar to the wakes in the lower branch/low-frequency state for the transverse cylinder oscillations.

The general features of the wakes before and after the jump persisted over the full range of flow and oscillation parameters examined in this study. Thus the general classification of the tethered cylinder system can be described in terms of two distinct wake states either side of the jump which we will call the low-amplitude state, occurring before the jump, and the upper state which occurs after the jump. Smaller subsets within these two states were also present, and further studies may reveal more; however, the jump appears to be the major feature of this system. The general characteristics of the states are as follows.

Low-amplitude state (*before the jump*). The wake exhibits the classic Kármán mode of vortex shedding, smaller layover angles, relatively small oscillation amplitudes with a small and almost constant drag coefficient.

Upper state (*after the jump*). The characteristic wake is non-symmetric with longer shear layers extending well across the wake centreline, higher layover angles, large oscillation amplitudes and higher drag coefficients.

The m^* regimes discussed in the previous section describe regions where the jump does and does not occur. At higher m^* values the jump did not occur, but as m^* approached unity especially periodic oscillations were observed at lower $Fr_{gravity}$ values. As $Fr_{gravity}$ increased, the motion was significantly less periodic, but averaged over many cycles the mean oscillation amplitude was of similar magnitude. Examination of mean vorticity fields in figure 9 at $m^* = 0.97$ shows that the periodic motion corresponds to an extremely short mean formation length whereas the less organized motion at higher $Fr_{gravity}$ values corresponds to a significantly longer mean formation length. A degree of asymmetry is evident in the mean wakes at $m^* = 0.97$, but in both cases the wake is consistent with the Kármán shedding mode before the jump.

Ongoren & Rockwell (1988) considered the forced oscillations of a cylindrical body at a range of angles to the flow direction. Although this study would appear to be relevant to the current study there is no overlap between the forced oscillation parameters and the observed oscillations of the tethered cylinder. The symmetric shedding mode observed by Ongoren & Rockwell was also not observed for the tethered system, perhaps suggesting that this mode is not stable for a freely oscillating system.

3.4. *Relationships between properties* – θ_{mean}, θ_{std}/θ_D, C_D

The results presented for lower mass ratios in the previous sections indicate that the jump corresponds to simultaneous changes in θ_{mean}, θ_{std}/θ_D and C_D, with the implication that these properties are interdependent. Equation (2) shows that the mean layover angle and the drag force are linked, as an increase in θ_{mean} corresponds to an increase in C_D and vice versa. Additionally, for an oscillating cylinder, an increase in the amplitude of oscillation is typically associated with an increase in C_D (e.g. see Sarpkaya 1978; Carberry *et al.* 2005). The current data set also shows a strong correlation between C_D and the oscillation amplitude. A simple explanation for this is that typically an increase in the amplitude of oscillation results in a wider wake, an increased momentum deficit and thus a corresponding increase in the mean drag force.

The displacement trace in figure 3(*c*) indicates that the transition from small values of θ_{mean}, θ_{std} and C_D to larger values of these parameters occurs after a short period during which the was consistent periodic motion and the small oscillations increased slightly in amplitude. Similarly, the transition in the opposite direction (figure 3*b*) appears to coincide with a point where the larger periodic oscillations were disrupted. These events are likely to correspond to changes in vortex shedding from the cylinder.

3.5. *Collapse of data*

In the preceding figures the response of the cylinder has been plotted against the non-dimensional Froude number $Fr_{gravity}$, representing the ratio of inertial and gravitational forces. Despite the fact that $Fr_{gravity}$ incorporates important components in the tethered body system, the data presented in figure 2 do not show a collapse of any of the response parameters. At this point we define a new Froude number which

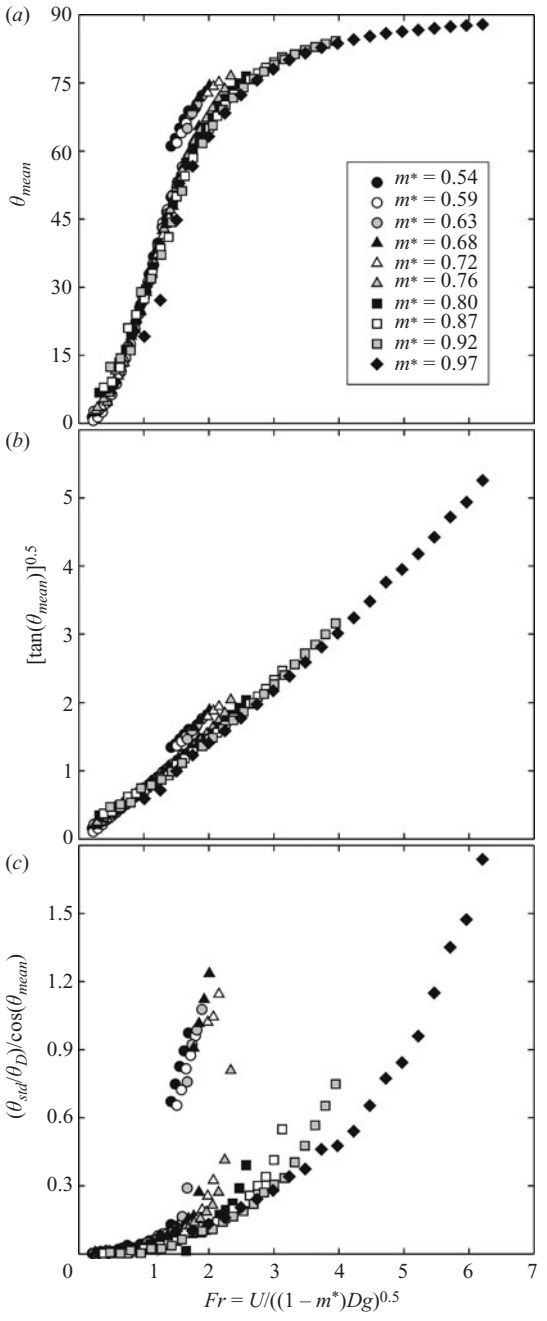

FIGURE 10. Variation with the buoyancy Froude no, $Fr = U/((1-m^*)gD)^{1/2}$ for $m^* = 0.54$ to 0.97 of (*a*) the mean layover angle, (*b*) $[\tan(\theta_{mean})]^{0.5}$ and (*c*) $(\theta_{std}/\theta_D)/\cos(\theta_{mean})$.

incorporates the buoyancy force into the vertical force component:

$$\left.\begin{array}{l} Fr_{bouyancy} \propto (\textit{fluid inertial force}/\textit{buoyancy force})^{0.5} \\ Fr_{bouyancy} = U/((1-m^*)gD)^{0.5} \\ (\text{for } m^* < 1). \end{array}\right\} \tag{4}$$

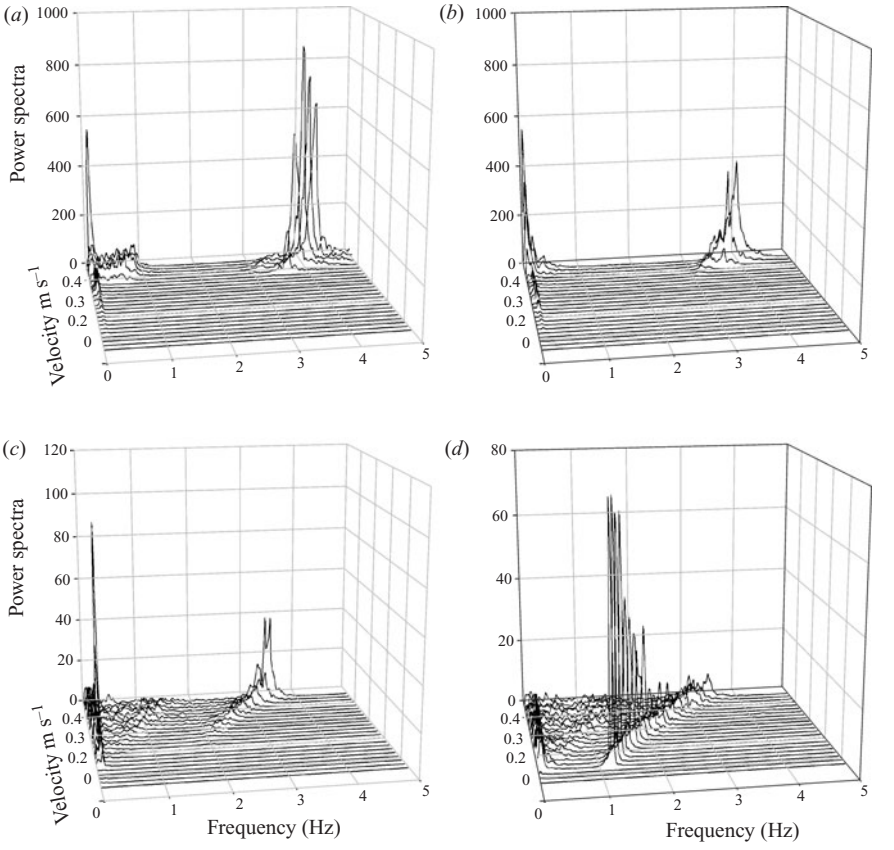

FIGURE 11. Variation of displacement spectra with free-stream velocity for (*a*) $m^* = 0.59$ representative of mass rations where the jump is observed; $0.54 \leqslant m^* \leqslant 0.72$, (*b*) $m^* = 0.72$, showing the change in the spectral energy at the end of the regime where the jump occurs, (*c*) $m^* = 0.87$ representative of mass rations where the jump does not occur; $0.76 \leqslant m^* \leqslant 0.87$ and (*d*) $m^* = 0.97$ representative of high mass rations as $m^* \to 1$.

$Fr_{buoyancy}$ represents the square root of the ratio of the fluid inertial and buoyancy forces and is hereinafter referred to as the Froude number, *Fr*.

When θ_{mean} is plotted against this new Froude number there is a very good collapse of the data onto two lines. The lower of these two lines (figure 10*a*), represents the data points before the jump at lower m^* and all points for $m^* \geqslant 0.76$ where the jump does not occur. The upper line corresponds to the points after the jump. This plot is consistent with the existence of two distinctly different states.

The collapse of the data shown in figure 10(*a*) is conceptually consistent with the balance of the mean force components in the direction normal to the tether, where this force balance forms the basis of (2). The simplest form of this force balance is,

$$Drag = Buoyancy \times \tan(\theta_{mean}).$$

If the drag force is directly related to the free-stream fluid inertial force then it follows that

$$\tan(\theta_{mean})^{0.5} = (Fluid\ inertia\ force / Buoyancy\ force)^{0.5} \propto Fr. \tag{5}$$

Plotting $\tan(\theta_{mean})^{0.5}$ against *Fr* gives an almost linear collapse of the two states (figure 10*b*). This indicates that for the two different states, the low-amplitude state

before the jump and the upper state after the jump, there is a nearly linear relationship between the drag force on the cylinder and the free-stream fluid inertial force. The gradient of the line through the data points after the jump in figure 10(*a*) is steeper than the line through the points corresponding to the low-amplitude state. This indicates that for the same inertial force ($\propto U\mathrm{d}U/\mathrm{d}x$) the upper state after the jump generates a higher drag coefficient, which is consistent with the data presented in figure 2(*d*).

The data presented in figure 10(*b*) does not incorporate the assumption that the mean lift force on the cylinder is zero; however, the force balances from which (2) and (5) are derived do incorporate this assumption. The data in figure 10(*b*), which considers the force components normal to the motion, conform well to the linear form predicted by (5), which indicates that the assumption of $C_L \approx 0$, while remaining a source of error, provides good physical insight.

Thus far we have focused on the mean layover angle using a static force balance approach. The other major response parameter is the amplitude of oscillation, represented by θ_{std}/θ_D. A wide range of parameters, including the mode and phase of vortex shedding, θ_{mean}, Re, as well as the energy transfer from the fluid to the cylinder may affect θ_{std}/θ_D. Thus, the reasonably good collapse of the data for the two states when $(\theta_{std}/\theta_D)/\cos(\theta_{mean})$ is plotted against Fr (figure 10*c*) is somewhat surprising and indicates that the properties of these states are robust. The collapse is better for low m^*, both before and after the jump, but is not as good for larger m^* particularly at higher free-stream velocities. Dividing by $\cos(\theta_{mean})$ resolves the oscillation amplitude into the direction of the free stream (i.e. into the axis of the force components in the Fr or into the drag direction). As discussed previously, there is a good correlation between θ_{std}/θ_D and C_D, thus plotting $C_D/\cos(\theta_{mean})$ against Fr gives a similar collapse to that observed in figure 10(*c*).

3.6. *Frequencies*

In § 3.2, the response of the cylinder was described in terms of three different m^* regimes. In figure 11, the variation of the spectral energy with U, where U varies directly with $Fr_{gravity}$, is shown for these regimes. The variation of the spectral energy, plotted for $m^* = 0.59$ in figure 11(*a*), is characteristic of the lower m^* regime, where the jump in θ_{mean}, θ_{std}/θ_D and C_D is observed; the change in the spectral energy as U increases through $0.38\,\mathrm{m\,s^{-1}}$ corresponds to the jump. Before the jump, there is a significant quantity of low-frequency energy which, in fact, dominates the energy at the frequencies associated with the small-scale oscillations shown in figure 3. The low-frequency peaks are consistent with the extensive modulation of the displacement trace at lower θ_{mean} values shown in figure 3(*a*). As m^* increases, there are systematic changes in the nature of the jump, summarized by figure 5. At the end of this regime, $m^* = 0.72$, the jump still corresponds to a sharp increase in the spectral energy at the oscillation frequency, but the peaks after the jump, shown in figure 11(*b*), become significantly more broadbanded.

The energy of the spectral peaks at both intermediate and high m^* values (figure 11*c*, *d*) is significantly less than the energy after the jump (note the difference in the vertical scale between figure 11*a* and figures 11*c* and 11*d*). At intermediate mass ratios ($0.76 \leqslant m^* \leqslant 0.87$) the energy at the oscillation frequency increases steadily with increasing U. The reason for the large low-frequency peak in figure 11(*c*) has not been fully determined; however, it may be due to resonance of the free surface water channel. Figure 11(*d*) clearly shows the difference between the motion of the cylinder as m^* approaches unity and the behaviour at other mass ratios. At low U

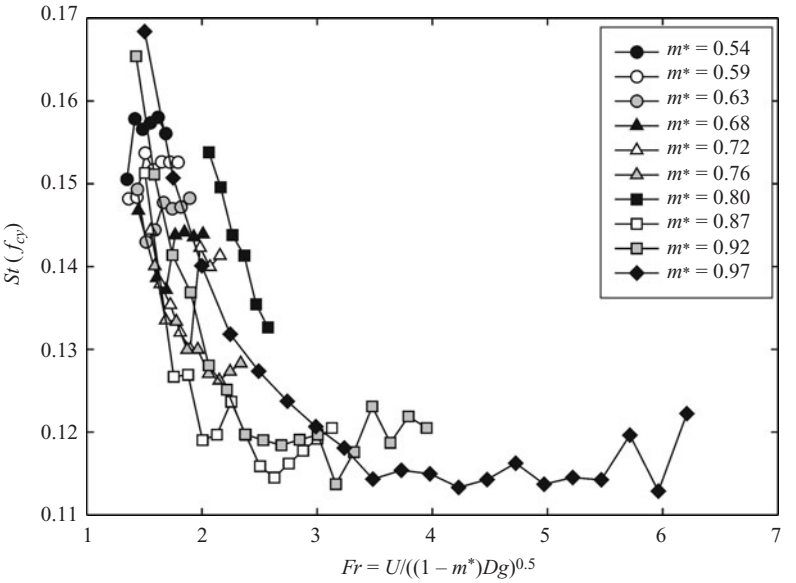

FIGURE 12. Variation of $St(f_{cyl})$ with the buoyancy Froude number for $m^* = 0.54$ to 0.97.

values, each spectrum has a sharp dominant peak at the oscillation frequency, where this peak corresponds to the highly periodic motion shown in figure 6(*a*). As U increases, the energy associated with this peak becomes more broadbanded and, as shown in figure 6(*b*), the motion is less organized although the standard deviation of $\theta(t)$ remains approximately constant.

In figure 12, the Strouhal numbers associated with the motion of the cylinder, $St(f_{cyl}) = f_{cyl}D/U$, i.e. the most energetic peaks in figure 11, are plotted as a function of $Fr_{buoyancy}$ and mass ratio. In all cases, the Strouhal number is significantly lower than the value for a stationary cylinder ($St(f_{Kármán}) \approx 0.20$–$0.21$). Additionally, for all cases the frequency at which the cylinder is oscillating is significantly greater than the natural structural frequency of the tethered cylinder, given by (3). Flow-induced vibrations often occur when the natural shedding frequency, which for a cylinder is typically taken as the Kármán frequency, is close to the natural structural frequency. However, in this case, the point at which $f_{Kármán} \approx f_N$ occurred before the onset of periodic motion at relatively low values of $Fr_{buoyancy}$, U and θ_{mean}. Moreover, once the cylinder begins oscillating the motion is not at the Kármán frequency. Thus, the motion of the cylinder does not appear to be linked to the resonance condition: $f_N \approx f_{Kármán}$. The relative magnitude of the cylinder's oscillation frequency $f_N < f_{cyl} < f_{Kármán}$ is consistent with the findings of Govardhan & Williamson (2000) for transverse cylinder oscillations, corresponding to $L^* = \infty$, at low m^* and higher reduced velocities well after the onset of motion.

After the jump, $St(f_{cyl})$ is essentially invariant with $Fr_{buoyancy}$ and increases with decreasing m^*. This is consistent with the trends observed by Govardhan & Williamson (2000) for the upper branch of their transverse cylinder oscillations. The Strouhal number decreases with increasing $Fr_{buoyancy}$ before the jump and also at lower $Fr_{buoyancy}$ for the low-amplitude state. At higher m^* and $Fr_{buoyancy}$ values, the oscillation frequency $St(f_{cyl})$ becomes less sensitive to changes in $Fr_{buoyancy}$, where in this region θ_{mean} is large and changes relatively little with increasing U.

4. Conclusions

This paper describes states of a tethered cylinder in a uniform free stream. The cases of an elastically mounted cylinder and a cylinder undergoing controlled oscillations are well documented; however, this is the first experimental investigation of a tethered cylinder. The direction of motion of a tethered cylinder relative to the free stream varies with layover angle, as do both the vectorial relationship between the force components on the cylinder and the natural structural frequency of the system. Despite the complexity of this system, the tethered cylinder exhibited two distinct states, the low-amplitude and upper states, which appear to be remarkably robust. In particular, the mean layover angle shows an excellent collapse when plotted against the Froude number, $Fr_{buoyancy}$. $Fr_{buoyancy}$ represents the ratio of the inertial force to the buoyancy force, as opposed to the traditional Froude number that uses the gravitational force instead of the buoyancy force. For the case of a tethered cylinder, and indeed any tethered body, when determining the form of the Froude number it is important to consider all of the force components on the body. Thus for the tethered cylinder, the Froude number, $Fr = Fr_{buoyancy} = U/((1 - m^*)gD)^{0.5}$, should be used to interpret the physical implications of the data, as evidenced by the fact that the data did not collapse when plotted against $Fr_{gravity}$. $Fr_{gravity}$, which varies linearly with the free-stream velocity, is used to represent the parameter varied during each set of experiments.

Significant oscillation amplitudes occur at all the mass ratios considered in this study, $0.54 \leqslant m^* \leqslant 0.97$. The motion is typically periodic in nature but, as is intuitively expected, the oscillations are less sinusoidal than those observed for purely transverse oscillations of a cylinder at similar Reynolds numbers. As $Fr_{gravity}$ increases, for lower m^* values, $0.54 \leqslant m^* \leqslant 0.72$, there is an abrupt jump in θ_{mean}, θ_{std}/θ_D and C_D. Before the jump, the cylinder's motion is small in amplitude with distinct long period beating and the wake is consistent with the classic 2S Kármán mode of shedding. These properties define the low-amplitude state.

After the jump, the upper state is characterized by significantly larger oscillation amplitudes, reaching peak values of $\theta_{max}/\theta_D \approx 0.6$, which are more periodic in nature. The upper state wake has long shear layers extending well across the wake centreline and is distinctly different from the Kármán wake before the jump.

At higher mass ratios, $m^* \geqslant 0.76$, the jump did not occur and the cylinder's oscillations, although increasing with increasing $Fr_{gravity}$, remain small and the wake remains in the Kármán mode, thus the system remains in the low-amplitude state. As m^* approaches unity at low flow velocities, the cylinder's motion is extremely periodic and the mean formation length is extremely short. In summary, the tethered cylinder has three different m^* regions which are characterized by the nature of the flow-induced motion, in particular whether or not the jump occurs as well as whether there are changes in the motion as $Fr_{gravity}$ and θ_{mean} increase. Defining m^*_{CRIT} as the mass ratio at which the jump first occurs we find that for $L^* = 0.46$, $m^*_{CRIT} = 0.74 \pm 0.02$.

The excellent collapse of θ_{mean} (figure 10*a*) combined with the surprisingly good collapse of the oscillation amplitude (figure 10*c*) provides further evidence supporting the existence of the two distinctly different states described above. The low-amplitude state is represented by the lower set of data points in these figures; while the upper set of data points represent the upper state. The collapse of this large amount of data into two states is consistent with the relatively constant drag coefficient for the two states and is remarkable considering the variation in the mean layover angle, oscillation amplitude and Reynolds number within each state.

This work was supported by Discovery Grant A10017086 from the Australian Research Council.

REFERENCES

Carberry, J., Govardhan, R., Sheridan, J., Rockwell, D. & Williamson, C. H. K. 2004 Wake states and response branches of forced and freely oscillating cylinders. *Eur. J. Mech.* B/*Fluids* **23**, 89–97.

Carberry, J. Sheridan, J. & Rockwell, D. 2005 Controlled oscillations of a cylinder: forces and wake modes. *J. Fluid Mech.* **538**, 31–69.

Govardhan, R. & Williamson, C. H. K. 2000 Modes of vortex formation and frequency response of a freely vibrating cylinder. *J. Fluid Mech.* **420**, 85–130.

Govardhan, R. & Williamson, C. H. K. 2002 Resonance forever: existence of a critical mass and an infinite regime of resonance in vortex-induced vibration. *J. Fluid Mech.* **473**, 147–166.

Govardhan, R. & Williamson, C. H. K. 2005 Vortex-induced vibrations of a sphere. *J. Fluid Mech.* **531**, 11–47.

Jauvtis, N. & Williamson, W. H. K. 2004 The effect of two degrees of freedom on vortex-induced vibration at low mass and damping. *J. Fluid Mech.* **509**, 23–62.

Ongoren, A. & Rockwell, D. 1988 Flow structure from an oscillating cylinder. Part 2. Mode competition in the near wake. *J. Fluid Mech.* **191**, 225–245.

Ryan, K. 2004 The analysis of wake structures behind stationary, freely oscillating and tethered cylinders. PhD thesis, Monash University.

Ryan, K., Thompson, M. C. & Hourigan, K. 2002 Energy transfer in a vortex induced vibrating tethered cylinder system. *Conference on Bluff Body Wakes and Vortex-Induced Vibrations, Port Douglas, Australia.*

Ryan, K., Thompson, M. C. & Hourigan, K. 2003 Flow-induced vibrations of a tethered circular cylinder. *IUTAM Symposium on Integrated Modelling of Fully Coupled Fluid–Structure Interactions Using Analysis, Computations, and Experiments, Rutgers, NJ, 6 June.*

Ryan, K., Pregnalato, C. J., Thompson, M. C. & Hourigan, K. 2004*a* Flow-induced vibrations of a tethered circular cylinder. *J. Fluids Struct.* **19**, 1085–1102.

Ryan, K., Thompson, M. C. & Hourigan, K. 2004*b* Vortex structures in the wake of a buoyant tethered cylinder at moderate to high reduced velocities. *Eur. J. Mech.* B/*Fluids* **23**, 127–135.

Sarpkaya, T. 1978 Fluid forces on oscillating cylinders. *J. Waterway Port Coastal Ocean Div.* **106**, 275–290.

Shiels, D., Leonard, A. & Roshko, A. 2001 Flow-induced vibration of a circular cylinder at limiting structural parameters. *J. Fluids Struct.* **15**, 3–21.

Zdravkovich, M. M. 1997 Flow around circular cylinders, vol. 1: Fundamentals. *Oxford University Press.*